

Modified Bose-Einstein condensation in an optical quantum gas

Mario Vretnar, Chris Toebes, and Jan Klaers*

Adaptive Quantum Optics (AQO), Complex Photonic Systems (COPS),

MESA⁺ Institute for Nanotechnology, University of Twente, PO Box 217, 7500 AE Enschede, Netherlands

(Dated: May 25, 2021)

Open quantum systems can be systematically controlled by making changes to their environment. A well-known example is the spontaneous radiative decay of an electronically excited emitter, such as an atom or a molecule, which is significantly influenced by the feedback from the emitter's environment, for example, by the presence of reflecting surfaces. A prerequisite for a deliberate control of an open quantum system is to reveal the physical mechanisms that determine the state of the system. Here, we investigate the Bose-Einstein condensation of a photonic Bose gas in an environment with controlled dissipation and feedback realised by a potential landscape that effectively acts as a Mach-Zehnder interferometer. Our measurements offer a highly systematic picture of Bose-Einstein condensation under non-equilibrium conditions. We show that the condensation process is an interplay between minimising the energy of the condensate, minimising particle losses and maximising constructive feedback from the environment. In this way our experiments reveal physical mechanisms involved in the formation of a Bose-Einstein condensate, which typically remain hidden when the system is close to thermal equilibrium. Beyond a deeper understanding of Bose-Einstein condensation, our results open new pathways in quantum simulation with optical Bose-Einstein condensates.

When a Bose gas exceeds the critical phase space density, a condensation process is triggered [1]. This process can be considered as a competition between various possible condensate wavefunctions that experience different growth rates under the given experimental conditions and in which ultimately the state with the highest rate prevails. If these growth rates are given by the respective Boltzmann factors, the system relaxes to thermal equilibrium and the condensation takes place in the state that minimises the energy. It is possible to modify these rates by moving to non-equilibrium conditions, for example, by controlling the particle exchange between the condensate and its environment. Intervening in the condensation process in this way is completely analogous to the modification of the spontaneous emission rate for quantum emitters by a deliberate control of dissipation and feedback from the environment [2, 3]. If the conditions for reaching thermal equilibrium are not met, the condensation will not necessarily occur in the lowest energy state. Beyond that, the question arises: Is it possible to formulate what kind of state a Bose condensate strives for under such non-equilibrium conditions? In contrast to cold atomic gases [4, 5], which typically do not allow significant particle exchange with their environment, optical quantum gases in photonic [6–16] and polaritonic [17–19] microcavity systems offer the possibility of answering such questions experimentally.

A Bose-Einstein condensed photon gas represents a source of coherent light that operates close to thermal equilibrium. Similar to a black-body radiator, a thermalisation process can be created by repeated resonant interactions between light and matter in a microcavity.

In contrast to a black-body radiator, however, the photon energy in such systems is significantly above the thermal energy, which effectively creates a non-zero chemical potential for the photons μ that is related to the excitation level in the optical medium by $e^{\frac{\mu}{kT}} \propto \rho_{\uparrow}/\rho_{\downarrow}$ [8]. Here, $\rho_{\uparrow,\downarrow}$ denote the densities of electronically excited and ground state molecules, which can be set by optically pumping the medium. A complete thermalisation process in the system would make all net energy and particle flows disappear. In real systems with imperfect photon confinement, the thermalisation process is not always able to bring the system into a global thermal equilibrium. This is especially true when highly inhomogeneous optical pump geometries are used. Such pump geometries can lead to non-equilibrium condensation phenomena in which the local chemical potential of the photons (understood as the local excitation level of the optical medium) varies across the system. This situation, however, still has to be differentiated from laser-like operation in which particle losses overcome photon reabsorption by the optical medium. The experiments described in this work are carried out in a parameter range in which the probability that a cavity photon is absorbed by the optical medium is significantly higher than the probability for transmission through the cavity mirrors, but not so high that the system relaxes into a global state of equilibrium with spatially homogeneous chemical potential irrespective of the optical pumping geometry.

A particular class of non-equilibrium condensation phenomena are transport processes, which are a current research topic in 2D optical quantum gases [20–23]. In these systems, condensates propagating in the transverse plane of the resonator can either be created by directly condensing into states with higher kinetic energy, or by preparing condensates at rest and subsequently setting

* j.klaers@utwente.nl

the particles in motion. To achieve the latter, the condensates must be generated in suitable potential landscapes using spatially inhomogeneous optical pump geometries. If the condensate is created at an elevated potential energy level, for example, particles will gain kinetic energy as they fall into regions of lower potential. This can be used to prepare a stream of photons in a controlled state of motion. In our experiments, such photon currents are directed into a potential landscape that acts as a Mach-Zehnder interferometer. By partially or completely closing the outputs of the interferometer, we can systematically vary the degree of dissipation and feedback in the system, which allows us to identify the underlying physical principles that determine the formation of Bose-Einstein condensates under non-equilibrium conditions.

Results

Experimental system. In our experiment, we use a high-finesse optical microcavity filled with a water-based solution of rhodamine 6G dye and the thermo-responsive polymer pNIPAM, in which the photons are repeatedly absorbed and re-emitted by the dye molecules, see Fig. 1. This process is governed by the Kennard-Stepanov law linking the (broadband) absorption coefficient $B_{12}(\omega)$ and the emission coefficient $B_{21}(\omega)$ by $B_{12}(\omega)/B_{21}(\omega) = \exp[(\hbar(\omega - \omega_{zpl})/kT)]$, where ω_{zpl} corresponds to the zero-phonon line of the dye and T denotes the temperature. Low cavity losses allow the photons to be absorbed and re-emitted multiple times before leaving the cavity, creating a thermalisation process between the photon gas and the dye solution. Indeed, Bose-Einstein distributed energies and the formation of Bose-Einstein condensates at room temperature have been demonstrated several times in this system [6, 7, 14, 24, 25]. The separation between the microcavity mirrors of $D_0 \simeq 10 \mu\text{m}$ is sufficiently small so that the longitudinal mode number becomes a conserved quantity in the interaction between the photons and the optical medium [6]. In this regime, the photon gas effectively becomes two-dimensional and the photon energy can be approximated by

$$E \simeq \frac{mc^2}{n_0^2} + \frac{(\hbar k_r)^2}{2m} - \frac{mc^2}{n_0^2} \left(\frac{\Delta d}{D_0} + \frac{\Delta n}{n_0} \right), \quad (1)$$

where k_r is the transversal wavenumber describing the two-dimensional motion in the cavity plane and m denotes the effective photon mass. The second and third term correspond to the kinetic and potential energy. The potential energy is non-vanishing, if the distance between the mirrors $D(x, y) = D_0 + \Delta d(x, y)$ or the refractive index $n(x, y) = n_0 + \Delta n(x, y)$ is modified across the transverse plane of the resonator (we assume $\Delta d \ll D_0$ and $\Delta n \ll n_0$).

Three different experimental techniques are combined to control the potential landscape within the microresonator. First, a static nanostructuring of the mirror surfaces of the cavity mirrors is performed via a direct laser

writing technique [26]. In this way, we can create smooth surface structures of up to 100 nm height with sub-nm precision in the growth direction. Second, a reversible tuning of the potential landscape is performed by locally heating the thermo-responsive polymer pNIPAM that is added to the optical medium with a short laser pulse [24]. The absorbed laser energy increases the local temperature of the optical medium by a few Kelvin such that it reaches the lower critical solution temperature (LCST) of pNIPAM in water (32°C). This leads to a significant increase of the index of refraction which, with eq. (1), translates into a tunable potential for the photons in the microcavity. Finally, the potential landscape can be further adjusted by tilting one of the mirrors, effectively adding a potential gradient to the photon gas.

In our experiments, we use non-resonant optical pumping to create regions of high chemical potential in which photon Bose-Einstein condensates form [see location 'high chemical potential' in 1a]. Particles emitted from the condensate into the microresonator plane are guided by two waveguide potentials. The waveguides are at a lower potential energy, which means that the condensate photons gain kinetic energy as they enter these regions. The two waveguides first guide the photons into disjoint areas of the microresonator plane before photons recombine in a region that is designed as a 50:50 beamsplitter. In the following, the waveguides between the condensate and the beamsplitter structure are referred to as the 'internal arms' of the interferometer, while the waveguides connected to the opposite end of the beamsplitter are referred to as 'output arms'. Optical path length differences between the internal arms of the interferometer can be generated with the help of the thermo-responsive optical medium. For this purpose, we heat the upper internal arm with a focused laser pulse, see location "heating" in Fig. 1a, so that the refractive index of the medium and thus the optical path length changes significantly. After the initial heating, the refractive index relaxes back to equilibrium. We observe that this decay is approximately exponential in time. Interestingly, the decay time is found to depend on the energy of the initial heating pulse. For sufficiently strong heating, it can become as large as a few seconds.

Open Mach-Zehnder interferometer. Results for self-interference experiments with photon BECs performed in this manner are shown in Fig. 1b. Here we show the photon density in the microresonator plane for different time delays between the initial heating pulse and the optical pumping. Depending on the probed path length difference, a switching between constructive and destructive interference in the outputs can be observed. This observation confirms the coherence of the particle stream emitted by the photon Bose-Einstein condensate [27]. Another indication is the interference pattern that arises when the waveguide potentials at the end of the two outputs cease, which is reminiscent of that of a double slit experiment. A quantitative characterisation of the system is obtained by determining the intensities $I_{1,2}$

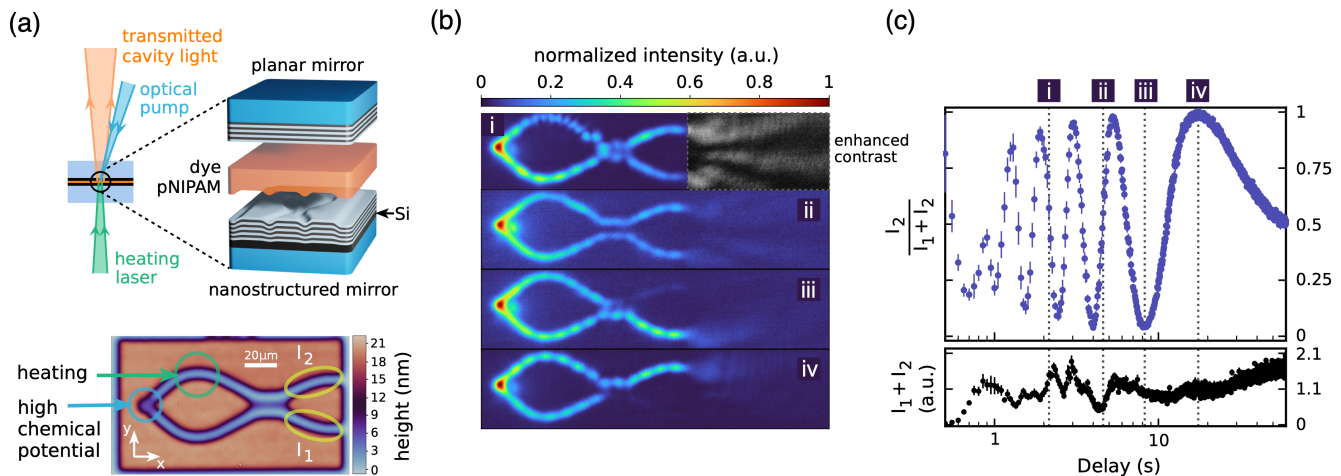


FIG. 1. **Photon Bose-Einstein condensation in an open Mach-Zehnder interferometer.** **a** Microcavity formed by a planar mirror, a nanostructured mirror, and an organic optical medium (top). The optical medium consists of a water-based solution of a dye (rhodamine 6G) and a thermo-responsive polymer (pNIPAM). The height profile of the nanostructured mirror (bottom), creates a potential landscape for the photon gas that effectively acts as a Mach-Zehnder interferometer. A laser beam at a wavelength of 532 nm is used to locally heat the thermo-responsive polymer. This allows for reversible tuning of the local refractive index, which can be used to create optical path length differences in the internal arms of the interferometer. The system is off-resonantly pumped with a tightly focused pulsed laser beam (pulse duration $\simeq 5$ ns, wavelength 470 nm). The time delay between the heating pulse and the optical pump pulse determines the path length difference that is probed. The photon density within the cavity is determined by measuring the transmitted cavity light with a camera. **b** Photon density for 4 time delays. **c** Normalised switching function $I_2/(I_1 + I_2)$ (upper graph) and total intensity $I_1 + I_2$ (lower graph) of the open interferometer as a function of the delay between heating and optical pumping. Data points are averages over 20 measurements (optical pulses). Error bars indicate the standard error of the mean.

in the lower and upper output arms of the interferometer [see locations ' I_1 ' and ' I_2 ' in Fig. 1a]. The upper graph in Fig. 1c shows the normalised intensity in the upper output arm $I_2/(I_1 + I_2)$ as function of the time delay. Every data point corresponds to an average over 20 optical excitations with a non-resonant pump pulse of $\simeq 5$ ns duration. These measurements demonstrate coherences close to 100% and a tuning range of more than 8π for the phase difference in the internal arms. The lower graph in Fig. 1c shows the total intensity integrated over both output arms as a function of time delay. Similar results as shown in Fig. 1 have previously been obtained in a related polaritonic system [28].

Semi-open Mach-Zehnder interferometer. In order to experimentally reveal the underlying physical principles determining the condensation process under non-equilibrium conditions, we will systematically vary the degree of dissipation and feedback in the system. For this purpose, we close one or even both output arms of the interferometer by creating additional potential walls at the ends of the waveguide potentials. Particles that reach these walls are reflected and propagate backwards through the interferometer. This backreflection eventually reaches the location of the Bose-Einstein condensate, where it interferes with the light field present there. Depending on the phase delays that the particles accu-

mulated on their way, the interference with the Bose-Einstein condensate can be constructive or destructive. Generally speaking, the condensation process is expected to be accelerated in the case of constructive interference, as this increases the local field amplitude, which triggers additional stimulated emission events. In contrast, destructive interference is expected to slow down the growth of the condensate. This feedback phenomenon is fully analogous to effects known from the modified spontaneous emission of quantum emitters [2, 3]. The feedback provided by the environment ultimately leads to a situation in which the condensation does not necessarily occur in the lowest energy state as suggested by a gain-loss rule of the Kennard-Stepanov type, but in a condensate state with higher kinetic energy for which the feedback from the environment is more favourable. In the Methods section we show that the initial evolution of the condensate population upon optical pumping can be approximately described by

$$\frac{\dot{n}}{n} = \Gamma_{\text{em}} - \Gamma_{\text{abs}} e^{\frac{\hbar(\dot{\theta} - \omega_0)}{kT}} - \Gamma_{\text{env}}(1 - \text{Re}[r(\dot{\theta})]), \quad (2)$$

where the condensate wavefunction is described by a single complex number $\psi = \sqrt{n} \exp(-i\theta)$ with time-dependent particle number $n = n(t)$ and phase $\theta = \theta(t)$. The interaction with the optical medium is mediated via stimulated absorption and emission with rates Γ_{abs}

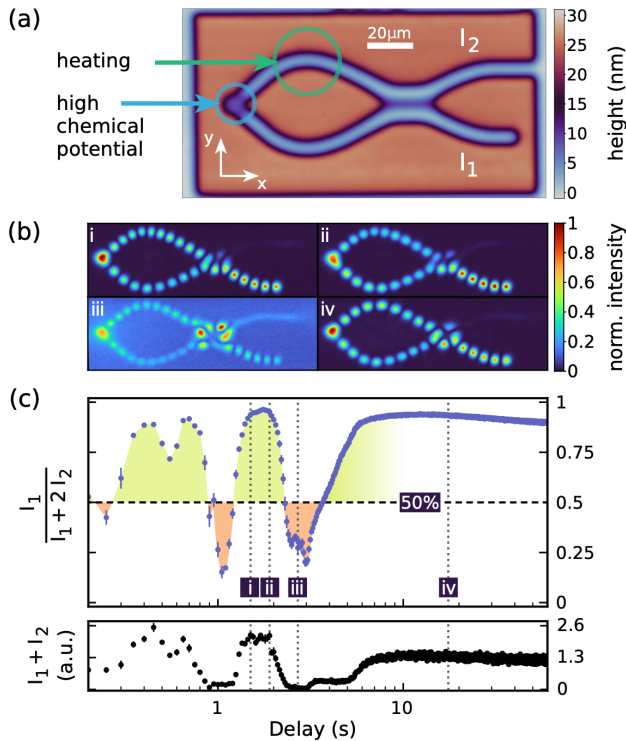


FIG. 2. **Semi-open Mach-Zehnder interferometer.** **a** Height map of the nanostructured mirror. **b** Normalized photon density for 4 specific time delays between the heating pulse in the upper internal interferometer arm ('heating') and the optical pumping ('high chemical potential'). The observed standing wave mode patterns indicate a superposition of an outgoing and a back reflected wave. **c** Normalised switching function $I_1/(I_1+2I_2)$ (upper graph) and total intensity I_1+I_2 (lower graph) of the semi-open interferometer. Data points are averages over 20 measurements (optical pulses). Error bars indicate the standard error of the mean.

and Γ_{em} . Furthermore, Γ_{env} denotes the rate of photons that are emitted from the condensate to the environment (interferometer), while the complex reflection coefficient $r = r(\theta)$ describes magnitude and phase delay of the coherent feedback created by the closed arm(s) of the interferometer. In general, the reflection coefficient depends on the frequency of the condensate θ as the propagation of particles through the interferometer is highly frequency-selective.

Closing the lower output arm (Fig. 2a) reflects the particle flow back through the interferometer and finally to the location of the Bose-Einstein condensate. In Fig. 2b we show intensity patterns obtained under these conditions for 4 different time delays after the initial heating pulse. A notable difference to the measurements with the open interferometer is the appearance of standing waves created by the superposition of forward and backward propagating waves. The distance between the nodes in the wave function can be taken as a measure of the velocity of the particles. The varying node distances in

the upper interferometer arm, see for example panel i in Fig. 2b, shows that the particles are first accelerated and then decelerated again when they run through the thermo-optically induced potential. In this way they obtain a different phase delay than the particles in the lower arm.

For the open interferometer the reflection amplitude r vanishes and the condensate growth rate $g = \dot{n}/n$ in eq. (2) reduces to the gain-loss rule originating from the Kennard-Stepanov law. In this case, the condensation occurs in the state that minimises the energy (vanishing kinetic energy) regardless of phase differences in the internal arms of the interferometer. This means that the switching function of the interferometer necessarily needs to assume a sinusoidal shape, as was indeed shown in Fig. 1c. Conversely, any deviation from a sinusoidal switching function indicates that the condensate energy is not a constant during the scanning of the interferometer and, consequently, that the condensation process is not solely determined by an energy minimisation rule. In the upper graph of Fig. 2c we show the normalised intensity in the lower (closed) output arm $\hat{I}_1 = I_1/(I_1+2I_2)$ as function of the time delay in the case of a semi-open interferometer. Since we compare the intensity of a traveling wave with that of a standing wave we have included an additional factor of 2 in the normalisation factor for compensating the additional intensity contribution of the back-propagating wave in the lower output arm. Interestingly, the switching function in Fig. 2c shows a clear imbalance between the intensities in the upper and lower output arms in favour of the intensity in the lower (closed) output. The latter refers not only to the maximum signal levels in both arms, but also to the time intervals for which $\hat{I}_1 > 0.5$. Even if one ignores the data for time delays of $t > 5$ s, since the refractive index of the medium is then largely relaxed, it is observed that the areas shaded in green ($\hat{I}_1 > 0.5$) occupy an area which is more than 4 times the size of the areas shaded in orange ($\hat{I}_1 < 0.5$). This imbalance shows in particular that the condensate energy is not constant while the interferometer is being scanned. Indeed, for the semi-open interferometer the condensate growth rate $g = \dot{n}/n$ in eq. (2) can be shown to favour condensate frequencies that increase the level of constructive interference in the closed arm, see Methods. As long as it does not become too detrimental in terms of energy (and the correspondingly stronger absorption by the optical medium), the condensate can adjust its kinetic energy in such a way that the particle loss via the open output arm is reduced. The same picture emerges from the behaviour of the total intensity I_1+I_2 , which is given as a function of time delay in the lower graph of Fig. 2c. The data indicates that the total intensity is significantly higher when the conditions for constructive interference in the closed arm are met (and vice versa). This simply means that the condensation process experiences a higher growth rate when the particle loss is reduced.

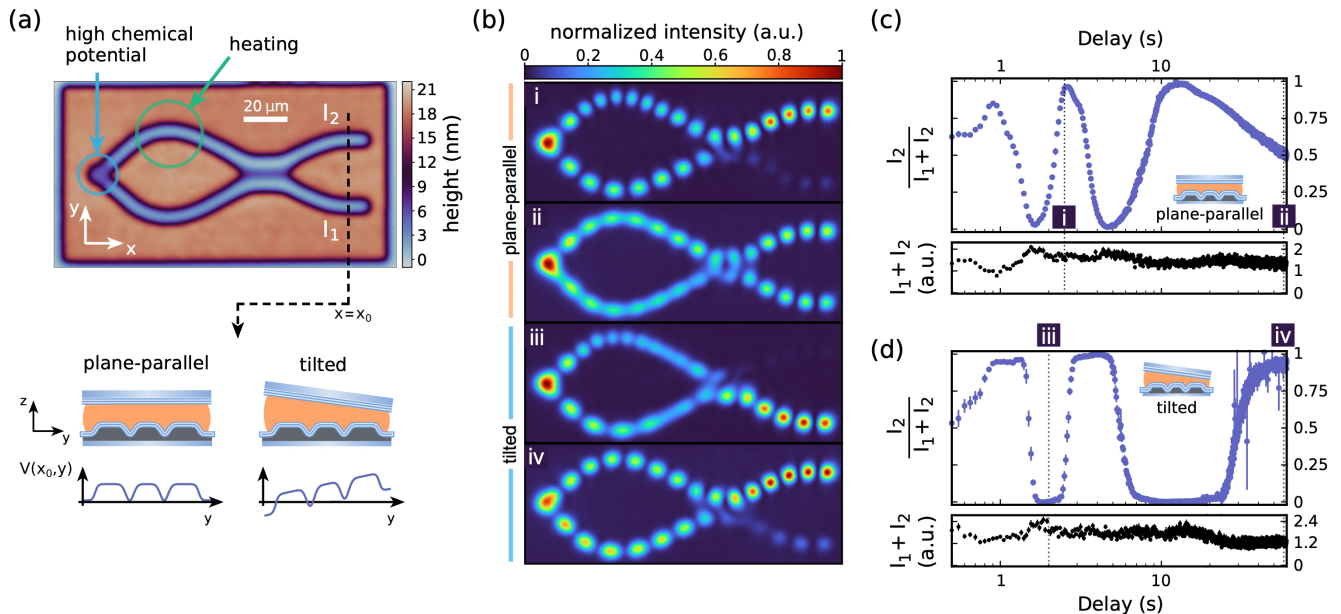


FIG. 3. **Closed Mach-Zehnder interferometer.** **a** Height map of the nanostructured mirror (top). For the results shown, the microcavity is operated in two configurations: plane-parallel and tilted. By tilting one of the microcavity mirrors, a potential gradient is introduced to the photon gas (bottom). This gradient leads to different phase delays for photons that propagate in the different output arms. **b** Normalised photon density at different time delays for both a plane-parallel and a tilted microresonator. **c** Normalised switching function $I_2/(I_1 + I_2)$ (upper graph) and total intensity $I_1 + I_2$ (lower graph) of the closed interferometer in plane-parallel configuration. **d** Normalised switching function $I_2/(I_1 + I_2)$ (upper graph) and total intensity $I_1 + I_2$ (lower graph) of the closed interferometer in a tilted configuration. Data points are averages over 20 measurements (optical pulses). Error bars indicate the standard error of the mean.

Closed Mach-Zehnder interferometer. For an interferometer that is closed at both output arms (see Fig. 3a), the particles emitted by the condensate return to the location of the condensation after passing through the interferometer twice (see the standing wave density profiles in Fig. 3b). These particles interfere with the condensate, which alters the rate of the condensation process. In the case where the optical path lengths in the two output arms are identical, the system has no reason to prefer constructive or destructive interference in either of the two output arms. Under these conditions, the switching function can be expected to return to the sinusoidal shape as in the case of the open interferometer, which can be confirmed experimentally, see Fig. 3c. The observation of shoulders in the otherwise sinusoidal shape of the switching function is related to transitions between wave functions with different numbers of nodes.

In the case that the optical path lengths in the output arms differ, a different scenario results. Differences in the optical path length of the outputs can be created by tilting one of the cavity mirrors. This effectively adds a potential gradient to the photon gas, which lifts the two output arms to two different potentials, see Fig. 3a. Due to the resulting optical path length difference, the feedback from the two output arms will not interfere in the

same way with the condensate. This means in particular that the feedback cannot be maximally constructive if the photon density is distributed over both interferometer outputs. Figure 3d shows experimental results for the case of a tilted cavity. The data presented in Fig. 3d reveal an almost discrete switching behaviour between maximum intensity in the upper and maximum intensity in the lower output arm as the phase difference between the internal arms of the interferometer is scanned. This demonstrates that the condensate adjusts its frequency in such a way that a maximum degree of constructive feedback is achieved for all optical path length differences.

Another interesting aspect related to the observed behaviour is the fact that the switching function becomes quite steep as it jumps between completely destructive and constructive interference. In these regions, the closed interferometer is highly susceptible to changes in optical path length - which is potentially interesting for sensing applications. Indeed, our measurement can be regarded as a special form of self-mixing interferometry [29, 30]. The observation that the switching functions for the plane-parallel and the tilted resonator are different, furthermore suggests that the interferometer can also be switched by changing the optical path length in the outputs. This is indeed confirmed experimentally, see Fig.

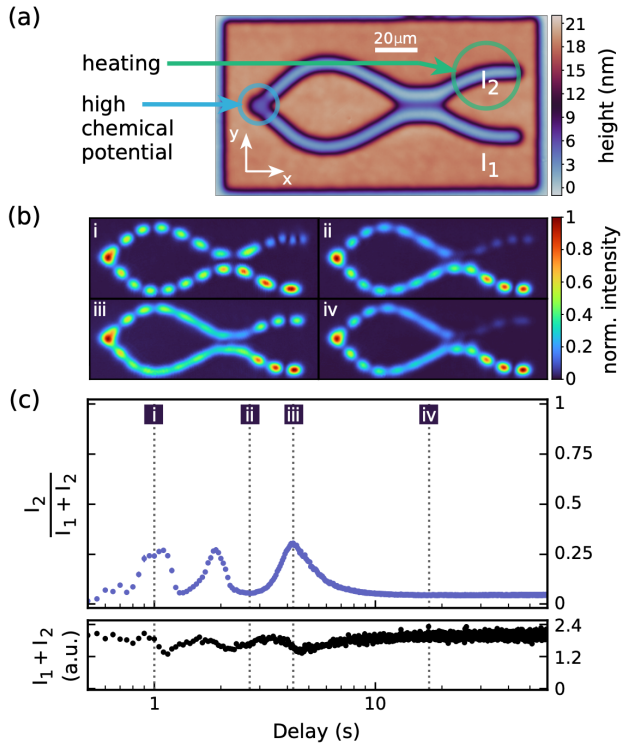


FIG. 4. **Closed Mach-Zehnder interferometer with optical path length tuning in the upper output arm.** **a** Height map of the nanostructured mirror. **b** Normalised photon density for 4 specific time delays between the heating pulse in the upper output arm ('heating') and the optical pumping ('high chemical potential'). **c** Normalised switching function $I_2/(I_1 + I_2)$ (upper graph) and total intensity $I_1 + I_2$ (lower graph) of the closed interferometer with output arm tuning. Data points are averages over 20 measurements (optical pulses). Errors are smaller than the symbol size.

4. The fact that the frequency of the condensate (and thus the relative intensities in the outputs) can be controlled by a refractive index change that is more than 100 micrometers away from the location of the condensation clearly demonstrates the 'non-local' character of the condensation process.

Conclusions

In conclusion, our work investigates the Bose-Einstein condensation of photons in a Mach-Zehnder interferometer potential with controlled dissipation and feedback. The switching behaviour of the interferometer is analysed in order to reveal the physical mechanisms that control the formation of a Bose-Einstein condensate. We show that by adjusting their frequency, Bose-Einstein condensates naturally seek to minimise particle loss and destructive interference in their environment. This ability remains hidden in thermal equilibrium, but becomes visible when the condensation occurs under non-equilibrium

conditions. Beyond a deeper understanding of Bose-Einstein condensation, our results open new pathways in novel computing schemes for the solution of hard optimisation problems based on coherent networks of photonic or polaritonic condensates [31, 32] and lasers [33, 34]. Understanding the physical mechanisms that determine the state of a condensate under controlled dissipation and feedback, as identified in our work, is essential to the design of such systems.

Acknowledgements

This work has received funding from the European Research Council (ERC) under the European Union's Horizon 2020 research and innovation programme (Grant agreement No. 101001512).

Methods

Experimental Methods. Our experiment is based on a high finesse dye microcavity as shown in Fig. 1. The mirror separation of $D_0 \simeq 10 \mu\text{m}$ is larger than in earlier photon BEC experiments. In general, short mirror spacings create experimental conditions in which the free spectral range of the resonator becomes larger than the emission bandwidth of the dye molecules. The longitudinal mode number then becomes a conserved quantity in the interaction between the photons and the optical medium. In our present experiments, we find that this is largely the case even at mirror distances where the free spectral range is comparable but not necessarily larger than the dye bandwidth. The advantage of working with a larger mirror spacing results from the reduced pump power required to trigger the condensation process and a lower susceptibility to imperfections in the nanostructuring of the mirror.

In the regime, in which the longitudinal mode number is frozen out, the photon gas becomes effectively two-dimensional. The photon energy in the cavity is given by

$$E = \frac{\hbar c}{n} \sqrt{k_z^2 + k_r^2}, \quad (3)$$

in which $n = n(x, y)$ describes the index of refraction and the longitudinal and transverse wavenumbers are denoted by k_z and k_r , respectively. The boundary conditions induced by the mirrors require $k_z = \pi q/D$, in which q is the longitudinal mode number and $D = D(x, y)$ denotes the mirror separation across the transverse plane. We assume that both $D(x, y)$ and $n(x, y)$ show only small variations across the cavity plane, i.e., $D(x, y) = D_0 + \Delta d(x, y)$ with $\Delta d(x, y) \ll D_0$ and $n(x, y) = n_0 + \Delta n(x, y)$ with $\Delta n(x, y) \ll n_0$. In a paraxial approximation ($k_r \ll k_z$), the photon energy in eq. (3) can be rewritten as

$$E \simeq \frac{mc^2}{n_0^2} + \frac{(\hbar k_r)^2}{2m} - \frac{mc^2}{n_0^2} \left(\frac{\Delta d}{D_0} + \frac{\Delta n}{n_0} \right), \quad (4)$$

where $m = \pi n_0 q / c D_0$ is the effective photon mass. The

first term corresponds to the rest energy of the (two-dimensional) photon, which is $mc^2/n_0^2 \simeq 2.1$ eV in our experiment (yellow spectral regime). The second term describes the (transverse) kinetic energy and the last term is the potential energy of the photons. The potential energy becomes non-zero, if either the mirror spacing or the refractive index changes locally. In our experiment, variations of the mirror distance can be created by nanostructuring one of the mirrors with a direct laser writing technique. With this technique, a laser scans over the backside of the mirror, locally heating an amorphous silicon layer located below the dielectric stack of the mirror. This causes an irreversible expansion of the silicon layer, pushing the dielectric stack outwards. In this way, we can create smooth surface structures of up to 100 nm height with sub-nm precision in the growth direction [26]. The height profiles of our mirrors are determined via Mirau interferometry. For these measurements, we use a commercially available interferometric microscope objective (20X Nikon CF IC Epi Plan DI).

The optical medium consists of a solution of rhodamine 6G in water (concentration 10 mmol/L) with a 4% mass fraction of the thermo-responsive polymer pNIPAM added. In our experiments, the dye molecules are excited by a pulsed optical parametric oscillator (OPO) with a pulse duration of $\simeq 5$ ns at a wavelength of 470 nm. This wavelength is outside the reflection band of the cavity mirrors and therefore allows non-resonant excitation on the optical axis. A second pulsed laser at a wavelength of 532 nm with pulse duration 10-20 ms is used to heat the silicon layer on the mirror. This leads to a temperature increase of a few Kelvin, which is enough to reach the lower critical solution temperature (LCST) of pNIPAM in water. This causes the polymer chains to collapse, which triggers a mass transport in the optical medium that locally changes the refractive index ($\Delta n \simeq 0.1$). In this way we can create variable potentials for the photon gas.

Theoretical Methods. The following section presents a theoretical model that reproduces the results observed in our experiments. An illustration of the model is given in Fig. 5. The wavefunction of the condensate is described by a single complex-valued amplitude ψ . This amplitude is affected by both the interaction with the optical medium, i.e. absorption and emission events, and the interaction with the environment. For the optical medium, we assume the validity of the Kennard-Stepanov law. We choose a particular implementation of the Kennard-Stepanov law, in which the emission coefficient of the medium is assumed to be frequency-independent and the absorption spectrum is assumed to increase exponentially with the frequency of the light. This corresponds approximately to the experimental conditions in our experiment. Taking this into account, we expect that the time evolution of the condensate can be described by the following dissipative Schrödinger equa-

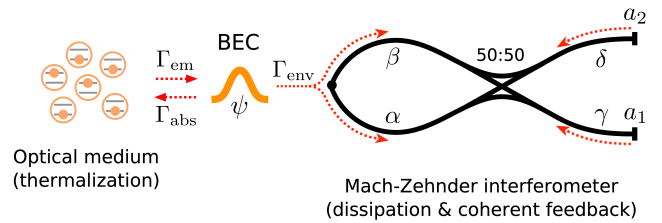


FIG. 5. **Theoretical model.** Our model describes the Bose-Einstein condensation of photons in an environment with controlled dissipation and feedback. A thermalization process is induced by absorption and emission processes in an optical medium. This competes with the coherent feedback from the environment, which is modelled as a Mach-Zehnder interferometer. The outputs of the interferometer are assumed to be either open or closed, which creates a varying degree of dissipation and feedback.

tion:

$$\frac{i\dot{\psi}}{\psi} = \omega_0 + \omega_r + \frac{i}{2} \left(\Gamma_{\text{em}} - \Gamma_{\text{abs}} e^{\frac{\hbar(\dot{\theta} - \omega_0)}{kT}} \right) - \frac{i}{2} \Gamma_{\text{env}} (1 - r(\dot{\theta})). \quad (5)$$

Here, ω_0 denotes the frequency of a condensate at rest, while ω_r accounts for a possible non-vanishing kinetic energy of the condensate. Γ_{em} and Γ_{abs} denote the emission and absorption rates. The particle exchange with the environment is described by the parameter Γ_{env} , which corresponds to the rate of particles that are emitted by the condensate to the Mach-Zehnder interferometer, and the reflection amplitude $r(\dot{\theta})$, which is a complex-valued function that describes magnitude and phase delay of the feedback created by the closed arm(s) of the interferometer. By describing the interferometer feedback as a complex multiple of the instantaneous wavefunction we implicitly have performed a slowly varying amplitude approximation for the time evolution of the condensate, i.e., we assume that the response time of the environment τ_{env} is so small that $|\dot{\psi}|/|\psi| \ll \tau_{\text{env}}^{-1}$. Here, τ_{env} corresponds to the time the photons need to travel back and forth through the Mach-Zehnder interferometer. Another approximation concerns the absorption (Γ_{abs}) and emission rates (Γ_{em}), which we assume to be constant at the initial formation of the condensate. This essentially means that eq. (5) only correctly describes the time evolution of sufficiently small condensates. The growth rate for the condensate population and the time evolution of the phase directly follow from eq. (5) by performing a transformation $\psi = \sqrt{n} e^{-i\theta}$ with real-valued functions $n = n(t)$ and $\theta = \theta(t)$:

$$\begin{aligned} \frac{\dot{n}}{n} &= \Gamma_{\text{em}} - \Gamma_{\text{abs}} e^{\frac{\hbar(\dot{\theta} - \omega_0)}{kT}} - \Gamma_{\text{env}} (1 - \text{Re}[r(\dot{\theta})]) \\ \dot{\theta} &= \omega_0 + \omega_r - \Gamma_{\text{env}} \text{Im}[r(\dot{\theta})]. \end{aligned} \quad (6)$$

In our experiments, the probabilistic character of the condensation process manifests itself in the fact that the condensate state can vary from shot to shot. In our

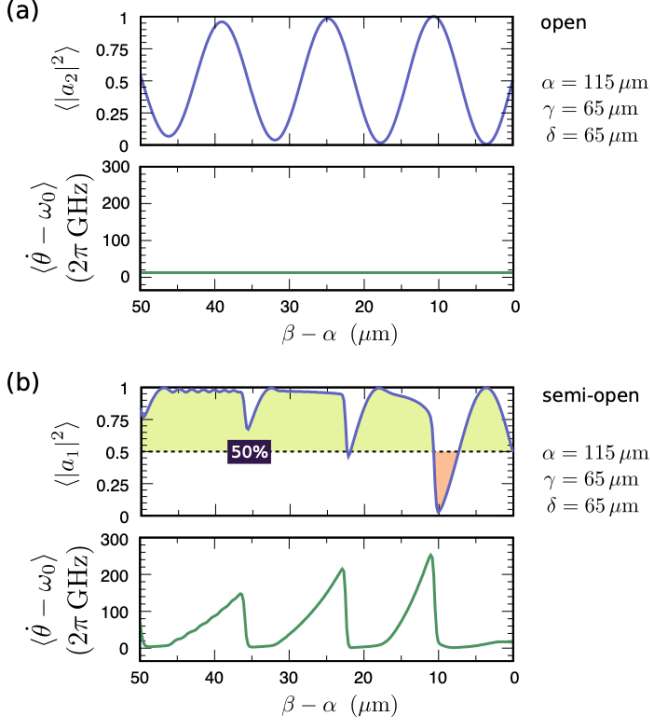


FIG. 6. Photon BEC in an open and semi-open Mach-Zehnder interferometer. Theoretically expected relative photon density in the output arms and mode frequency as a function of the optical path length difference. **a** Open MZI. **b** Semi-open MZI. Parameters used to calculate these graphs are $\hbar\omega_0 = 2.1$ eV, $m = 6.8 \cdot 10^{-36}$ kg, $T = 300$ K, $D_0 = 10$ μm , $\Delta d = 4.5$ nm, $\Gamma_{\text{abs}} = 100$ GHz, $\Gamma_{\text{env}} = 6.3$ GHz, and $t^* = 4.75$ ns. All other relevant parameters are given in the figures. Note that some parameters such as Γ_{em} have no influence on the calculation of the expectation values shown here.

model, we can introduce this kind of randomness by converting the growth rate function $g = \dot{n}/n$ in eq. (6) into a probability distribution. To do this, we define the probability for the occurrence of a condensate with frequency $\dot{\theta}$ as $p(\dot{\theta}) = \exp(g(\dot{\theta})t^*)/Z$, where $g(\dot{\theta})$ is the growth rate of the state, t^* is an effective time parameter, and Z is a normalization parameter such that $\int p(\dot{\theta})d\dot{\theta} = 1$. Furthermore, an expectation value for an observable Q can be defined as $\langle Q \rangle = \langle Q \rangle_{t^*} = \int p(\dot{\theta})Q(\dot{\theta})d\dot{\theta}$. Similar to the temperature in thermal averages, the time parameter t^* determines the statistical composition of the expectation value. For small values of t^* , many different states contribute almost equally to the average, while for large values of t^* the statistical average is dominated by the state that maximizes the growth rate. In the following, we use the time parameter as a global free parameter, which is chosen to obtain the best match between model and experiment. It turns out, however, that the found value of this parameter is close to the actual pulse duration.

In order to reproduce the experimental results with the help of the so-defined model, the frequency-dependent reflection amplitude $r = r(\dot{\theta})$ has to be determined. For

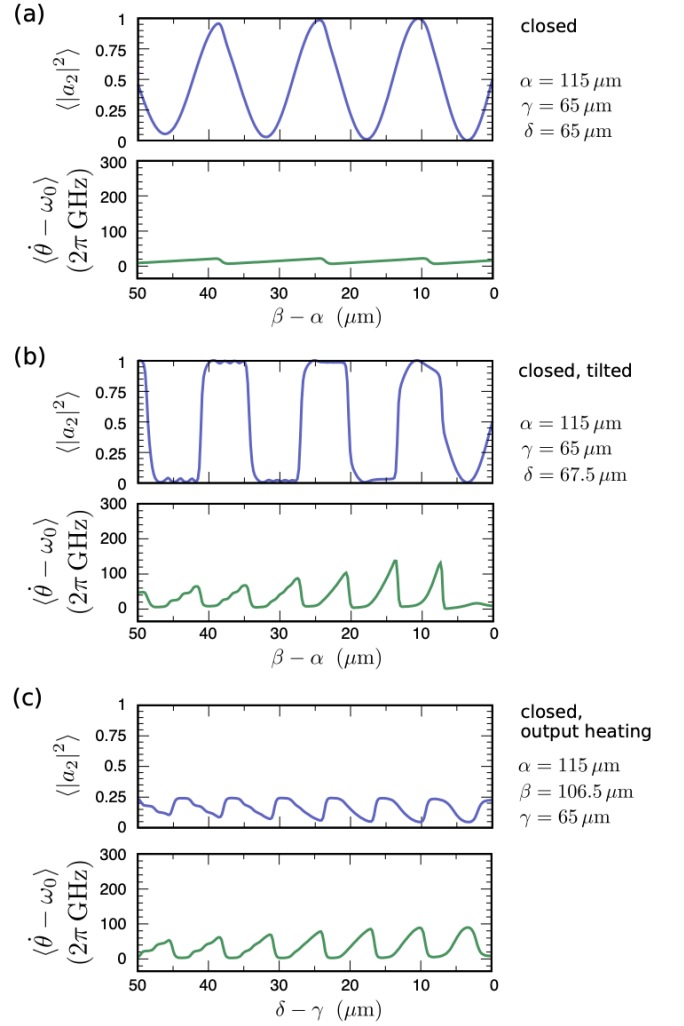


FIG. 7. Photon BEC in a closed Mach-Zehnder interferometer. Theoretically expected relative photon density in the output arms and mode frequency as a function of the optical path length difference. **a** Closed MZI in plane-parallel configuration. **b** Closed MZI in tilted configuration. **c** Closed MZI, for which the optical path length tuning is performed in the upper output arm. Parameters used to calculate these graphs are the same as in Fig. 6.

the open interferometer, this amplitude simply vanishes: $r_{\text{open}} = 0$. In general, r is obtained by adding up the probability amplitudes of all possible paths through the interferometer, which both start and end at the condensate. As an intermediate step, we determine the probability amplitudes at the two outputs of the interferometer, which, assuming a perfect 50:50 beamsplitter, are given by $a_1 = (i e^{ik(\alpha+\gamma)} + e^{ik(\beta+\gamma)})/2$ and $a_2 = (e^{ik(\alpha+\delta)} + i e^{ik(\beta+\delta)})/2$. Here, α , β , γ , and δ denote the optical path lengths of the 4 interferometer arms, see Fig. 5. The wavenumber $k = k(\dot{\theta})$ of the photons propagating in the interferometer arms follows from $k = (2m[\dot{\theta} - \omega_0(1 - \Delta d/D_0)]/\hbar)^{1/2}$, where $\Delta d \simeq 4.5$ nm denotes the height difference between the condensate lo-

cation and the interferometer arms on the nanostructured surface of our mirror (drop in potential energy). With this, the frequency-dependent reflection amplitude in the semi-open interferometer (output 1 closed, output 2 open) becomes $r_{\text{semi}} = -a_1 a_1$. For the closed interferometer, we obtain $r_{\text{closed}} = -a_1 a_1 - a_2 a_2$.

Figures 6 and 7 show results for the expected relative photon densities in the output arms of the interferometer $\langle |a_{1,2}|^2 \rangle$ (upper graphs) and the mode frequency $\langle \hat{\theta} - \omega_0 \rangle$ (lower graphs) as a function of the optical path length difference. For the open interferometer, our model reproduces the expected sinusoidal variation of the output intensity. No variation of the condensate frequency is predicted. For the semi-open interferometer, the imbalance in the switching function predicted by our model is even more pronounced than in the experimental data

in Fig. 2. For large path length differences, this imbalance increases, which suggests that, from a certain threshold value, the photon density is fully concentrated in the closed interferometer output regardless of the optical path length difference in the internal interferometer arms. In order to direct the particle flow into the closed interferometer arm, the frequency of the condensate can adapt to a certain extent, see lower graph in Fig. 6b. For the closed interferometer, our theoretical model shows a transition between sinusoidal and rectangular switching functions, depending on the path length difference in the output arms. This is in good agreement with our experimental results shown in Fig. 3. Qualitative agreement is furthermore obtained for the closed interferometer with optical path length tuning in the upper output arm, see Fig. 7c and Fig. 4.

-
- [1] A. Griffin, D. W. Snoke, and S. Stringari, *Bose-Einstein condensation* (Cambridge University Press, 1996).
- [2] K. Drexhage, Influence of a dielectric interface on fluorescence decay time, *Journal of Luminescence* **1-2**, 693 (1970).
- [3] P. Lodahl, A. Floris van Driel, I. S. Nikolaev, A. Irman, K. Overgaag, D. Vanmaekelbergh, and W. L. Vos, Controlling the dynamics of spontaneous emission from quantum dots by photonic crystals, *Nature* **430**, 654 (2004).
- [4] M. H. Anderson, J. R. Ensher, M. R. Matthews, C. E. Wieman, and E. A. Cornell, Observation of Bose-Einstein condensation in a dilute atomic vapor, *Science* **269**, 198 (1995).
- [5] K. B. Davis, M. O. Mewes, M. R. Andrews, N. J. van Druten, D. S. Durfee, D. M. Kurn, and W. Ketterle, Bose-Einstein condensation in a gas of sodium atoms, *Phys. Rev. Lett.* **75**, 3969 (1995).
- [6] J. Klaers, F. Vewinger, and M. Weitz, Thermalization of a two-dimensional photonic gas in a ‘white wall’ photon box, *Nat. Phys.* **6**, 512 (2010).
- [7] J. Klaers, J. Schmitt, F. Vewinger, and M. Weitz, Bose-Einstein condensation of photons in an optical microcavity, *Nature* **468**, 545 (2010).
- [8] J. Klaers, J. Schmitt, T. Damm, F. Vewinger, and M. Weitz, Statistical physics of bose-einstein-condensed light in a dye microcavity, *Phys. Rev. Lett.* **108**, 160403 (2012).
- [9] P. Kirton and J. Keeling, Nonequilibrium model of photon condensation, *Phys. Rev. Lett.* **111**, 100404 (2013).
- [10] P. Kirton and J. Keeling, Thermalization and breakdown of thermalization in photon condensates, *Phys. Rev. A* **91**, 033826 (2015).
- [11] J. Schmitt, T. Damm, D. Dung, F. Vewinger, J. Klaers, and M. Weitz, Thermalization kinetics of light: From laser dynamics to equilibrium condensation of photons, *Phys. Rev. A* **92**, 011602(R) (2015).
- [12] J. Marelic and R. A. Nyman, Experimental evidence for inhomogeneous pumping and energy-dependent effects in photon Bose-Einstein condensation, *Phys. Rev. A* **91**, 033813 (2015).
- [13] H. J. Hesten, R. A. Nyman, and F. Mintert, Decondensation in nonequilibrium photonic condensates: When less is more, *Phys. Rev. Lett.* **120**, 040601 (2018).
- [14] B. T. Walker, L. C. Flatten, H. J. Hesten, F. Mintert, D. Hunger, A. A. P. Trichet, J. M. Smith, and R. A. Nyman, Driven-dissipative non-equilibrium Bose-Einstein condensation of less than ten photons, *Nat. Phys.* **14**, 1173 (2018).
- [15] V. N. Gladilin and M. Wouters, Vortices in nonequilibrium photon condensates, *Phys. Rev. Lett.* **125**, 215301 (2020).
- [16] F. E. Öztürk, T. Lappe, G. Hellmann, J. Schmitt, J. Klaers, F. Vewinger, J. Kroha, and M. Weitz, Observation of a non-Hermitian phase transition in an optical quantum gas, *Science* **372**, 88 (2021).
- [17] Y. Sun, P. Wen, Y. Yoon, G. Liu, M. Steger, L. N. Pfeiffer, K. West, D. W. Snoke, and K. A. Nelson, Bose-Einstein condensation of long-lifetime polaritons in thermal equilibrium, *Phys. Rev. Lett.* **118**, 016602 (2017).
- [18] T. Cookson, K. Georgiou, A. Zasedatelev, R. T. Grant, T. Virgili, M. Cavazzini, F. Galeotti, C. Clark, N. G. Berloff, D. G. Lidzey, and P. G. Lagoudakis, A yellow polariton condensate in a dye filled microcavity, *Advanced Optical Materials* **5**, 1700203 (2017).
- [19] T. K. Hakala, A. J. Moilanen, A. I. Väkeväinen, R. Guo, J.-P. Martikainen, K. S. Daskalakis, H. T. Rekola, A. Julku, and P. Törmä, Bose-Einstein condensation in a plasmonic lattice, *Nat. Phys.* **14**, 739 (2018).
- [20] T. Jacqmin, I. Carusotto, I. Sagnes, M. Abbarchi, D. D. Solnyshkov, G. Malpuech, E. Galopin, A. Lemaître, J. Bloch, and A. Amo, Direct observation of dirac cones and a flatband in a honeycomb lattice for polaritons, *Phys. Rev. Lett.* **112**, 116402 (2014).
- [21] D. Ballarini, D. Caputo, C. S. Muñoz, M. De Giorgi, L. Dominici, M. H. Szymańska, K. West, L. N. Pfeiffer, G. Gigli, F. P. Laussy, and D. Sanvitto, Macroscopic two-dimensional polariton condensates, *Phys. Rev. Lett.* **118**, 215301 (2017).
- [22] O. Jamadi, E. Rozas, G. Salerno, M. Milićević, T. Ozawa, I. Sagnes, A. Lemaître, L. Le Gratiet, A. Harouri, I. Carusotto, J. Bloch, and A. Amo, Direct observation of photonic landau levels and helical edge states in strained honeycomb lattices, *Light: Science & Applications* **9**, 144 (2020).

- [23] J. D. Töpfer, H. Sigurdsson, L. Pickup, and P. G. Lagoudakis, Time-delay polaritonics, *Communications Physics* **3**, 2 (2020).
- [24] D. Dung, C. Kurtscheid, T. Damm, J. Schmitt, F. Vewinger, M. Weitz, and J. Klaers, Variable potentials for thermalized light and coupled condensates, *Nat. Photonics* **11**, 565 (2017).
- [25] S. Greveling, K. L. Perrier, and D. van Oosten, Density distribution of a Bose-Einstein condensate of photons in a dye-filled microcavity, *Phys. Rev. A* **98**, 013810 (2018).
- [26] C. Kurtscheid, D. Dung, A. Redmann, E. Busley, J. Klaers, F. Vewinger, J. Schmitt, and M. Weitz, Realizing arbitrary trapping potentials for light via direct laser writing of mirror surface profiles, *EPL* **130**, 54001 (2020).
- [27] J. Schmitt, T. Damm, D. Dung, C. Wahl, F. Vewinger, J. Klaers, and M. Weitz, Spontaneous symmetry breaking and phase coherence of a photon Bose-Einstein condensate coupled to a reservoir, *Phys. Rev. Lett.* **116**, 033604 (2016).
- [28] C. Sturm, D. Tanese, H. S. Nguyen, H. Flayac, E. Galopin, A. Lemaître, I. Sagnes, D. Solnyshkov, A. Amo, G. Malpuech, and J. Bloch, All-optical phase modulation in a cavity-polariton Mach-Zehnder interferometer, *Nat. Commun.* **5**, 3278 (2014).
- [29] M. Rudd, A laser doppler velocimeter employing the laser as a mixer-oscillator, *Journal of Physics E: Scientific Instruments* **1**, 723 (1968).
- [30] G. Giuliani, M. Norgia, S. Donati, and T. Bosch, Laser diode self-mixing technique for sensing applications, *Journal of Optics A: Pure and Applied Optics* **4**, S283 (2002).
- [31] N. G. Berloff, M. Silva, K. Kalinin, A. Askitopoulos, J. D. Töpfer, P. Cilibrizzi, W. Langbein, and P. G. Lagoudakis, Realizing the classical XY Hamiltonian in polariton simulators, *Nat. Mater.* **16**, 1120 (2017).
- [32] M. Vretenar, B. Kassenberg, S. Bissesar, C. Toebes, and J. Klaers, Controllable Josephson junction for photon Bose-Einstein condensates (2020), arXiv:2001.09828 [cond-mat.quant-gas].
- [33] M. Nixon, E. Ronen, A. A. Friesem, and N. Davidson, Observing geometric frustration with thousands of coupled lasers, *Phys. Rev. Lett.* **110**, 184102 (2013).
- [34] T. Inagaki, K. Inaba, R. Hamerly, K. Inoue, Y. Yamamoto, and H. Takesue, Large-scale Ising spin network based on degenerate optical parametric oscillators, *Nat. Photonics* **10**, 415 (2016).